RÔYAL SOCIETY OF CHEMISTRY

Soft Matter

ARTICLE

Decomposition vs. Escape of Topological Defects in a Nematic Liquid Crystal

Received 00th January 20xx, Accepted 00th January 20xx

DOI: 10.1039/x0xx00000x

www.rsc.org/

Bryce S. Murray^a, Samo Kralj^b, and Charles Rosenblatt^a

Nematic cells patterned with square arrays of strength $m=\pm 1$ topological defects were examined as a function of cell thickness (3 < h < 7.5 μ m), temperature, and applied voltage. Thicker cells tend to exhibit an escape of the nematic director as a means of mitigating the elastic energy cost near the defect cores, whereas thinner cells tend to favor splitting of the integer defects into pairs of half-integer strength defects. On heating the sample into the isotropic phase and cooling back into the nematic, some apparently split defects can reappear as unsplit integer defects, *or vice versa*. This is consistent with the system's symmetry, which requires a first order transition between the two relaxation mechanisms.

1 Introduction

Topological defects (TDs) exist throughout nature. They occur on length scales that range from subatomic particles to cosmological 1 , and exhibit universal behaviors that do not depend on the particular details of the system. Given their convenient length and time scales, their ubiquitous phases, and their ease of experimental visualization, liquid crystals long have served as a test bed for investigations of TDs^2 . In the nematic phase, for which there is orientational but no long-range translational order of the molecular long axis, TDs can occur as point, linear, or planar singularities in one, two, or three dimensions, at which the orientation of the uniaxial nematic director \widehat{n} becomes ill-defined.

In recent years strides have been made in creating very small patterned TDs in liquid crystals, which have facilitated studies requiring stable, pinned defects. Ackerman, Qi, and Smalyukh have used an optical technique to create 3D patterns of electrically erasable "torons", with spacings as small as 10–20 μ m [Ref. 3]. Guo, et al developed a plasmonic photopatterning technique to create arbitrary patterns for planar liquid crystal alignment on length scales of tens of micrometers⁴. Our group recently developed the method of scribing a polymer-coated substrate using an atomic force microscope (AFM) stylus to create planar TD patterns on similar length scales, including arrays of line TDs that have high defect "strength" m [Refs. 5,6]. Here m is defined as $\Delta\theta/2\pi$, where θ is the nematic director's azimuthal angle with respect to an arbitrary axis and $\varDelta\theta$ the director's total angular change on circumnavigating the defect line. (Later, we shall choose

Topological defects entail a strain energy cost, which can be relaxed by several mechanisms, including decomposition of an integer defect into pairs of half-integer defects⁵ or by escape of the director into the third dimension^{7,8}. In a theoretical study, Chiccoli⁹, et al estimated the free energy of a pair of strongly anchored (split) half-integer defects to be $F_{pair} = \pi K d \left[\frac{1}{2} ln(2R^2/rL) + 2u \right]$, where K is an elastic constant; d is the cell thickness; R is a characteristic domain size, e.g., the spacing between our patterned integer defects; L is the gap separating the split defects; r is a molecular size; and u is the normalized defect core energy. For a fully escaped integer defect they calculated the energy to be $F_{esc} =$ $\pi Kd[ln(R/d)+g]$, where g is a universal constant ~ 4.1. The logarithmic dependence and similar functional forms render the operative escape mechanism weakly sensitive to d, and also dependent on the anchoring strength and elastic anisotropies, neither of which is included explicitly in the model. Within the context of their approximations, Chiccoli, et al^9 found that $m = \pm 1$ defects in uniaxial nematic cells always escape for cell thickness d > 200 to 500 nm; defect splitting, i.e., decomposition, does not occur. They also found that escape tends to occur for weakly biaxial nematics, but splitting into pairs of half-integer defects takes place when biaxiality is strong. The latter result is consistent with experimental work by Smalyukh, et al, who found that defect decomposition occurs in a biaxial Smectic-A phase¹⁰, although escape cannot occur due to the constraints of the smectic layers. In this work we exploit the AFM scribing approach to create regular arrays of topological line defects in thin liquid crystal cells, which we examine using polarized microscopy as functions of applied electric field and cell thickness. We observe a number of behaviors. We find that thinner cells (cell thickness $d \sim 3 \mu m$) tend to favor decomposition of integer defects into pairs of half integer defects, i.e., of strength $m = \pm \frac{1}{2}$. On application of an electric field along the direction normal to the substrates, a

this axis to the polarizer orientation.)

^a Deptartment of Physics, Case Western Reserve University, Cleveland, Ohio 44106 USA

^{b.} Department of Physics, Faculty of Natural Sciences and Mathematics, University of Maribor, Koroška cesta 160, SI-2000 Maribor, Slovenia and Jožef Stefan Institute, P.O. Box 3000, SI-1000 Ljubljana, Slovenia

sharp Freedericksz transition generally is observed, whereby dI/dV changes abruptly with increasing voltage V in the region just outside the central defect cores; here I is the intensity of the transmitted polarized light. Thicker cells ($d > 6 \mu m$) tend to favor escape of the nematic director outside the defect core^{7,8}, as indicated by the absence of a well-defined Freedericksz transition threshold in these regions. However, both decomposition and escape behavior can occur in the same cell, and the behaviors can interchange after the liquid crystal is heated into, and cooled back from, the isotropic phase

Our preliminary theoretical analysis using a minimal Landau-de Gennes type approach with a tensor nematic order parameter suggests that for our patterned $m=\pm 1$ defect arrays in cells a few micrometers thick, either a split defect (in thinner cells) or an escaped defect (in thicker cells) structure can exist. (Note that the tensor nematic order parameter admits the possibility of biaxiality as yet another strain relief mechanism. These configurations are separated by a discontinuous structural transition on increasing the cell thickness. In the following we describe our experimental findings, which are consistent with outcomes of our preliminary theoretical analysis. Details of the theory will be published elsewhere 14 .

2 Experiment

Let us turn to the experiments. A 3 x 3 two-dimensional array of alternating m=+1 and -1 topological defects (Fig. 1) was patterned onto a thin layer of polyvinyl alcohol (PVA) that had been deposited onto an indium-tin-oxide (ITO)-coated glass substrate, a method similar to that described in detail in Ref. 5. [We note that in our previous work^{5,6} we had used the polyamic acid RN-1175 (Nissan Chemical Industries).] The stylus of an atomic force microscope was used to scribe the square defect array, in which each defect was separated by 30 μ m from its nearest neighbors. Here the defect in the center

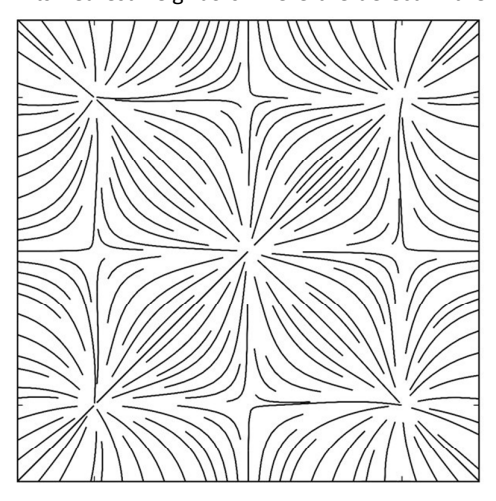


Fig. 1 Schematic representation of easy axis pattern for a 3 x 3 square array of $m=\pm 1$ defects, with $m=\pm 1$ defect in the center. For purposes of clarity, note that the line spacing shown is much larger than the actual scribing pattern.

of the 3 x 3 array was chosen to have a strength m = +1. A second ITO-coated glass substrate was cleaned and spincoated with polymethyl methacrylate (PMMA, $M_w = 97,000$) and baked at 80°C for 120 min. The coating provides good planar-degenerate alignment surface for the liquid crystal director¹⁵, and serves as a "slave" surface to the patterned PVA "master" surface. The two substrates were placed together, separated by Mylar spacers, and wires were attached to the two semitransparent ITO layers, which facilitated application of an electric field across the liquid crystal sandwich. Two cells were prepared, one having a gap of $d = 3.1 \mu m$ and one wedged cell containing four patterns at locations having gaps of d = 3.9, 4.9, 6.5, and 7.5 μ m. The gap thicknesses d of the wedged sample were determined by interferometric measurements and have an uncertainty of $\pm 0.2~\mu m$. The gap thickness of the 3.1 μm sample was determined by examining the total retardation of the transmitted light. Each cell was filled with the liquid crystal pentylcyanobiphenyl (5CB) in the isotropic phase, cooled to room temperature, and placed on the stage of a polarizing microscope with a 20x objective. Imaging was accomplished using a high resolution (5616 x 3744 pixels) CCD array. A set of measurements was made at room temperature as a function of applied voltage for all gaps d, and another set for the d = 3.1 $\mu \mathrm{m}$ gap at zero applied voltage, but by varying temperature through the nematic phase.

Figure 2 shows images of the four patterns in the wedged cell, with the first column being transmission micrographs with crossed polarizer and analyzer, and the second column the corresponding bright field images with the analyzer removed. Note that all measurements, unless otherwise indicated, were made in the nematic phase at approximately 30 °C. Splitting of the $m = \pm 1$ integer defects into pairs of half-integer defects are discerned more easily in the bright field images, in which the dark spots correspond to light scattered away from the detection optics by the defect cores. The separations between the split $m = \pm \frac{1}{2}$ defects tend to be a few micrometers, which is due to a tradeoff between the mutual repulsion of defects of the same sign and the underlying substrate patterning, which prevents them from moving too far from the patterned integer defect core. The separation can be different at the two substrates due to their different anchoring conditions; this will be addressed below.

Let us now turn to images obtained on application of a voltage across the sample. For these and all subsequent measurements we placed a narrow bandpass filter centered at wavelength $\lambda=515$ nm and having a passband $\Delta\lambda=10$ nm in the optical path. A voltage V was applied to the cell, ramped from 0 to 3.5 V over a period 80 minutes. Images up to 0.7 V were obtained at voltage steps of 0.005 V, followed by voltage steps of 0.01 V. A frame was taken approximately once every 12 s. At higher voltages domain walls were found to move through the pattern and, as a result, we limited our data analysis to voltages below 1.4 V.

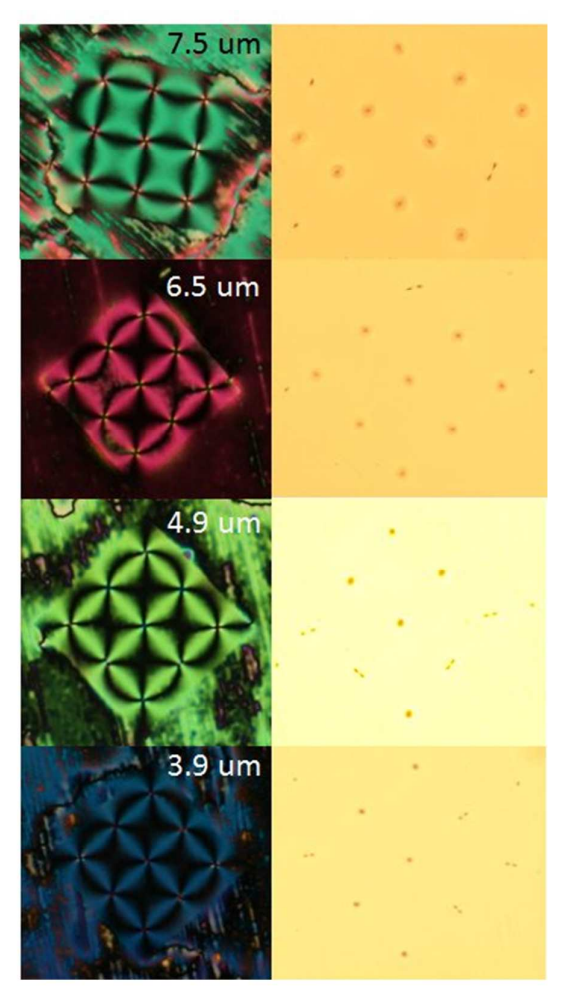


Fig. 2 Polarizing microscope images (left column) using white light for illumination and bright field images (right column) of patterns in wedged cell at different thicknesses. Spacing between patterned $m = \pm 1$ defects is 30 μ m. Uncertainty in cell thickness is 0.2 μ m. Polarizer/analyzer directions are parallel to the edges of each of the square patterns.

For each pattern, the images were arranged in a 3D "stack" using Image-J software ¹⁶, with the x- and y-axes corresponding to the spatial position in the image. The z-axis in the stack corresponds to the applied voltage V, *i.e.*, each image in the stack corresponds to a given voltage. Arranging the images in this way allows us to select an arbitrary location in the xy-plane and extract the intensity value at that same point on each image through the stack to create a voltage profile, as shown in Fig. 3c for the points in Figs. 3a and 3b, corresponding to the $d=3.1~\mu{\rm m}$ cell. (The scale bar in every figure corresponds to 5 $\mu{\rm m}$). Figure 4c, which corresponds to the same cell as Fig. 3 but which highlights a different defect, shows the extracted voltage profiles corresponding to the locations in Fig. 4a and 4b. Another useful representation is

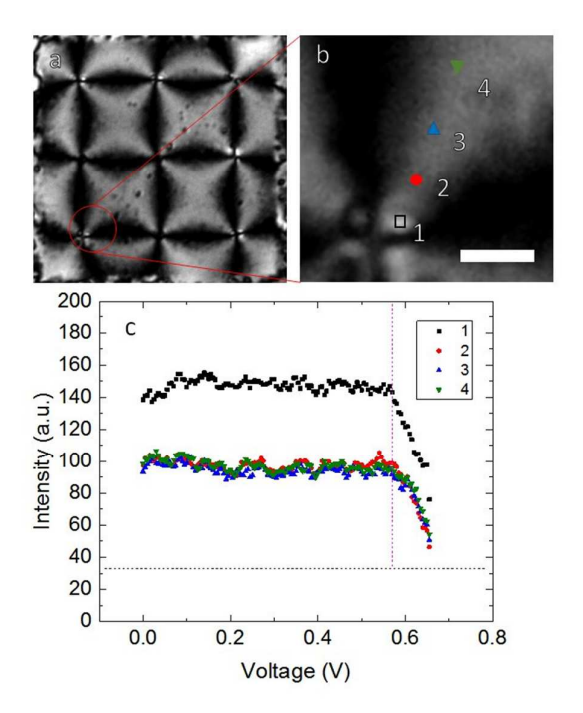


Fig 3 a) Polarizing microscope image of $d=3.1~\mu m$ thick cell using light of wavelength $\lambda=515$ nm for illumination at V = 0. Polarizer/analyzer directions are parallel to the edges of the square pattern. b) Split defect: Enlargement from a), showing the locations where voltage profiles were taken. Scale bar is 5 μm . c) Plot of intensity vs. voltage at the positions shown by the markers in Fig. 3b. The horizontal dashed line corresponds to the experimental background intensity.

shown in Fig. 5, where we extract the intensity data at every point along the yellow lines for every image in the stack. Figures. 5b and 5c display the grayscale intensity, with the distance along the yellow line as the vertical axis and the applied voltage as the horizontal axis. Figures 6 through 10, corresponding to other thicknesses, are treated as in Fig. 3. We note that the units of the intensity axis are arbitrary, and cannot be compared directly among Figs. 3c, 4c, and 6c through 10c.

We remark that all of our intensity measurements have a small nonzero offset due to a combination of detector noise, polarizer quality, and imperfections in the substrates. We show this offset in Figs. 3c by a horizontal dashed line, which was obtained by measuring the intensity in a region where the nematic director is parallel to the polarizer and at an elevated temperature at which the optical retardation $\alpha = 2\pi$. Data sets for the other sample thicknesses are shown in Figs. 6 through 9, in order of increasing sample thickness, although in these samples the offset is not shown in the intensity vs. voltage plots.

3 Discussion

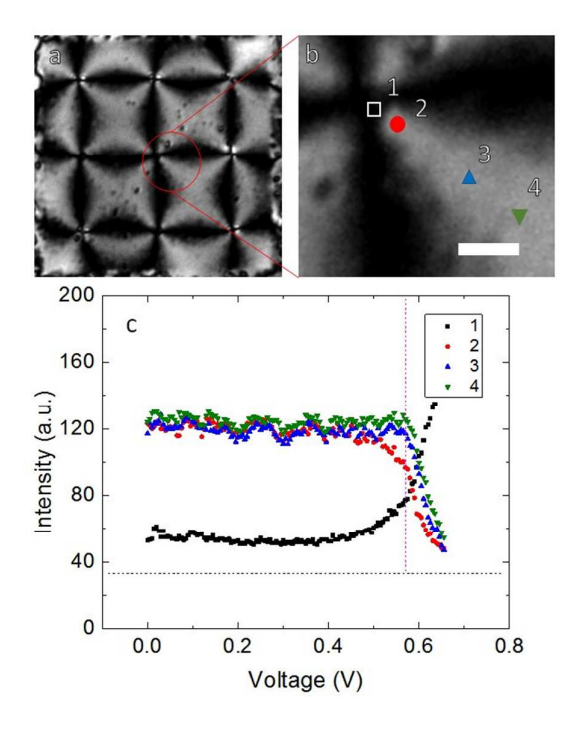


Fig 4 Same as Fig. 3, except the analysis is performed near the central escaped defect. Scale = 5 µm

Examination of the images reveals a somewhat ambiguous situation in that both unsplit $m=\pm 1$ defects and $m=\pm \frac{1}{2}$ defects can be observed for all sample thicknesses d, and correspond to escaped defects and split defects, respectively; this observation is consistent with symmetry and the discontinuous nature of the transition from one configuration to the other. Examining the images in more detail, the bright field images in Fig. 2 suggest that splitting into half-integer defects is less prevalent for the two thicker spacings, where eight of the nine integer defects in each sample are not obviously split and show a relatively large dark spot. The two narrower spacings, on the other hand, show four obviously split defects, as well as a number of others that are smaller than the dark spots in the thick samples and are peanutshaped. This peanut shape suggests either splitting into halfinteger defects where the distances are comparable to - or smaller than — the diffraction limitation, or an escaped integer defect in which the boojums at the top and bottom surfaces do not line up vertically. Note that we have observed arrays in a thin cell in which every defect was split into a pair of halfinteger defects.

In the work presented herein, a contributory factor to defect splitting is the imperfect nature of the central regions of each patterned defect core. The scribing-induced easy axis will necessarily have some minimum length scale, below which it is unable to orient the liquid crystal with a singularity at the center of the topological defect. The edges of this scribed region act as a boundary condition, and the innermost core area relaxes to its minimum energy with, at most, a perturbation of the director orientation from a symmetric

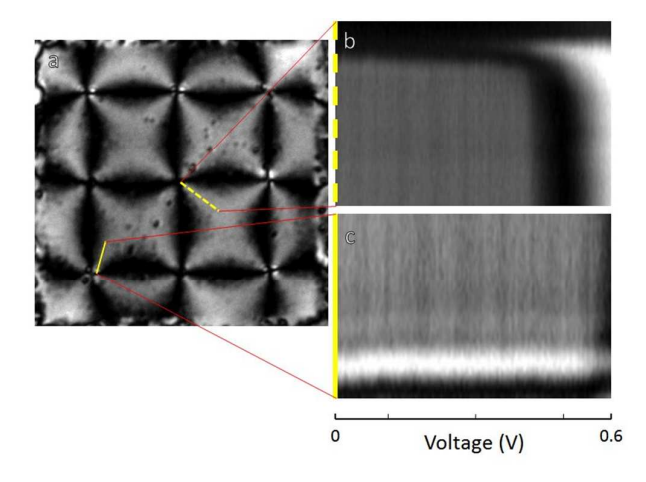


Fig 5 Two voltage re-slices. a) Polarizing microscope image of $d=3.1~\mu m$ cell, same image as Figs 3a and 4a. The solid line shows the location of the slice taken near the split defect, while the dashed line shows the same for the escaped defect. b) Profile of an escaped defect. Intensity shown in gray scale as a function of position along the dashed yellow line in Fig. 5a (vertical axis) vs. applied voltage (horizontal axis), with V=0 on the left. c) Same as in b), except for the solid yellow line near the split defect.

defect due to imperfections at the surface. This favorable configuration is a pair of half integer defects that repel each other as far as the patterned easy axis will allow. We also note that on heating the sample into the isotropic phase and cooling back into the nematic, some apparently split defects can reappear as unsplit integer defects, *or vice versa*. This observation is in line with our preliminary theoretical analysis 14 , which suggests the first order structural transition between the escaped defect and split defect structure on varying d. Consequently, a bistability regime must exist, giving rise to the observed hysteresis behavior. We note that because of the typically small biaxial correlation length of $^{\sim}30$ – 50 nm associated with calamitic nematics 13 , optical observation of the biaxial region is not possible using standard optical microscopy.

Other issues also may influence the tendency for integer defects to split or remain whole but escaped, including anchoring strength, patterning resolution, and sample irregularity. We discussed irregularity in the previous paragraph. Some effects of anchoring strength in our experimental geometry have been discussed qualitatively in Refs. 9 and 10 where, in particular, weaker polar anchoring for a planar-aligned director tends to promote escape behavior. Both polar and azimuthal anchoring strengths have been measured for an AFM-scribed substrate as a function of line resolution¹⁷. However, the quantitative consequences of finite anchoring on the behavior of topological defects, especially the various mechanisms for strain relaxation, are still being investigated theoretically⁶, which renders possible only qualitative explanations.

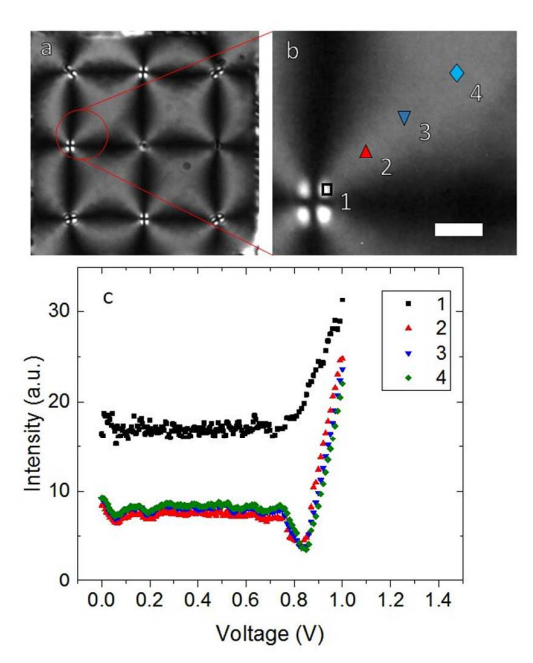


Fig 6 Same as Fig. 3 except for d = 3.9 μm . The defect of interest is split into half-integer defects. Scale = 5 μm

We now consider the behavior of the topological defects as a function of applied voltage V. Examination of the intensity vs. position and V (Fig. 3 and Figs. 6 through 10) reveals a qualitative difference between escaped defects in thin and thick cells. Moreover, we see a qualitative difference between split and escaped defects. For split defects, the change of intensity on increasing the voltage can occur sharply and at approximately the same value of V for all positions away from the central defect core. These data are shown in Figs. 3c, 6c, and 10c in the form of a Freedericksz transition-like curve. At positions away from these cores, the intensity vs. voltage traces reveal a clear Freedericksz transition, which indicates a minimal degree of pretilt angle at the two substrates and absence of escaped behavior. We point out that, within experimental uncertainty, the actual Freedericksz threshold voltage varies systematically with cell gap, being smallest for the d = 7.5 μ m cell and largest for the d = 3.9 μ m cell. This is explained quantitatively by the capacitive impedance: A significant voltage drop occurs across the alignment layers owing to their thickness δ > 300 nm at each of the two substrates, and the approximately factor of three ratio for the relative permittivities of the liquid crystal to that of the alignment layers. Note that the threshold voltage for the thinnest gap, $d = 3.1 \mu m$, stems from a different cell with a somewhat thinner alignment layer.

Let us now turn to escaped defects. As the cell gap increases, the behavior of escaped defects begins to change qualitatively. Here there is some washing out and curvature of the transition band from dark to light in the position vs. voltage images (Fig. 5b), especially moving closer to the defect core. Moreover, the intensity does not change quite as sharply with increasing voltage as it does in the thinner cells, as is apparent in Fig. 7c on moving toward the defect core.

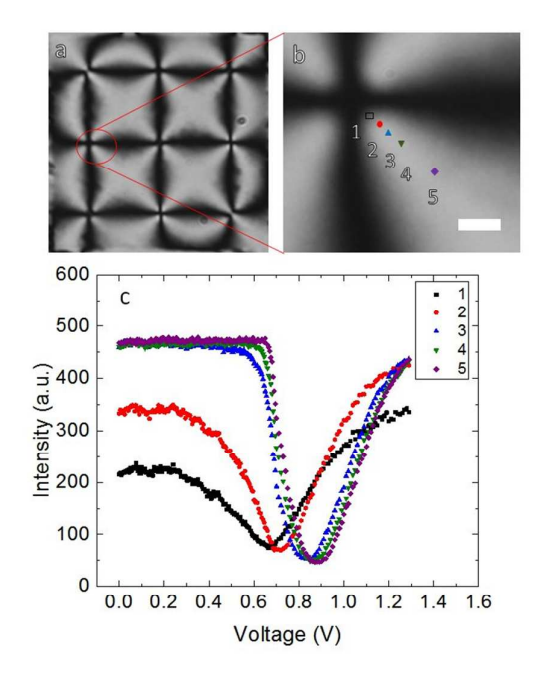


Fig 7 Same as Fig. 3 except for d = 4.9 μm . b) and c) refer to an escaped defect. Scale = 5 μm

These two behaviors are even more apparent for the wider gaps in Figs. 8c and 9c. Of course, as the cell gap d grows, the total change in optical retardation grows concomitantly, and one expects more peaks and troughs to appear in the voltage profiles (like Fig. 5b and 5c) far from the defect cores, as is observed. The intensity vs. voltage plots in Figs. 8c and 9c reveal an absence of a clear Freedericksz transition close to the core, and can be explained by an escape of the director

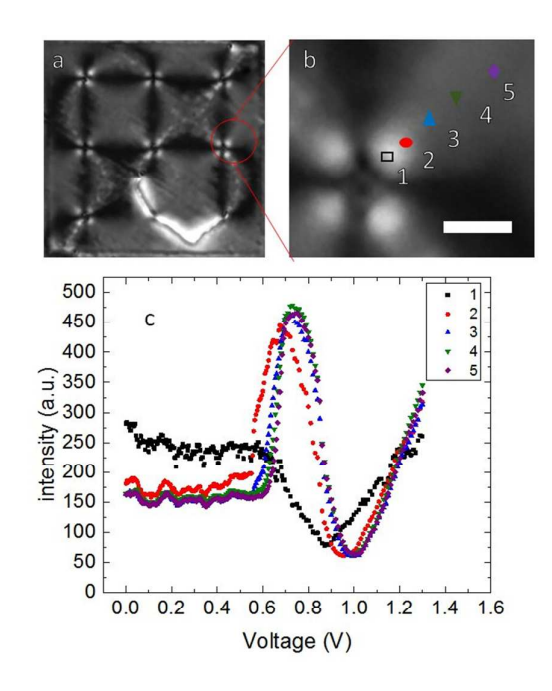


Fig. 8 Same as Fig. 3 except for $d=6.5~\mu m$. Notice domain wall has appeared in Fig. 8a. b) and c) refer to an escaped defect. Scale = 5 μm

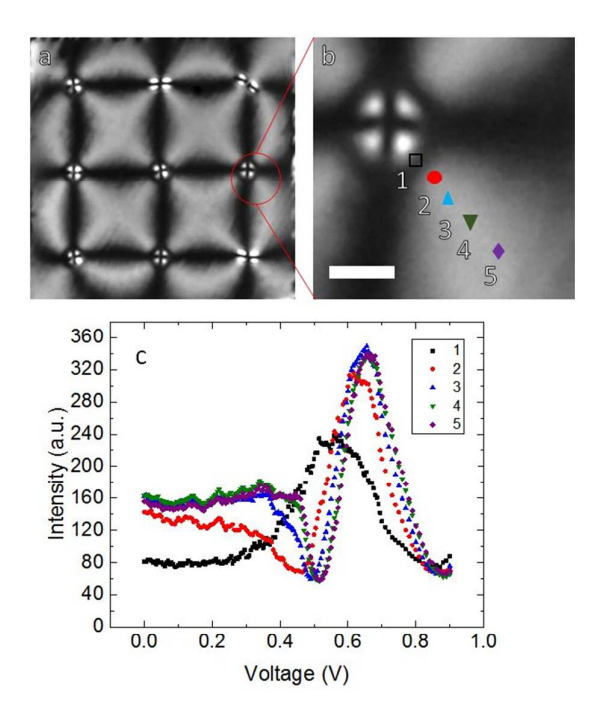


Fig. 9 Same as Fig. 3 except for d = 7.5 μ m. b) and c) refer to an *escaped* defect. Scale = 5 μ m

along the direction of the cell normal, especially closer to the defect core region. This escaped behavior is not surprising, and was predicted for uniaxial nematics in Ref. 9.

We show in Fig. 10 the behavior of a split defect in a thick $d=7.5~\mu m$ cell. Examining points along the symmetry axis but perpendicular to the splitting, we see that the voltage data (Fig. 10c) is qualitatively similar to that of the split defect in a much thinner sample, with clear Freedericksz-like behavior and thus no apparent escape of the director.

For all cell spacings d, we observe that there are four regions (or discrete diffraction-limited spots) around and close to every $m = \pm 1$ defect or $m = \pm \frac{1}{2}$ defect pair, which generally have a different intensity than the immediately adjacent liquid crystal in the inter-defect regions, i.e., along the diagonal between defect cores. In many cases, particularly in thicker samples, these four spots are surrounded by a dark ring; see, e.g., Fig. 9a. Here the dark crosses between these bright spots are due to the crossed polarizer and analyzer. For sufficiently thick cells, the dark ring is a signature of escaped behavior or partially escaped behavior when anchoring is stiff -of the nematic director: $\alpha > 2\pi n$ in the planar inter-defect region (where n is an integer), α passes through $2\pi n$ in the dark ring as the director escapes along the z-axis, and falls below $2\pi n$ in the bright spots around the defect cores as the z-component of the director continues to increase closer to the escaped core. That only one dark ring is observed for thicker cells (Figs. 8 and 9) indicates that the escape behavior is only partial, and that the director makes an oblique angle with the substrate normal in the defect core region. In Fig. 11 we show a series of images for an m = -1 partially escaped defect as a function of

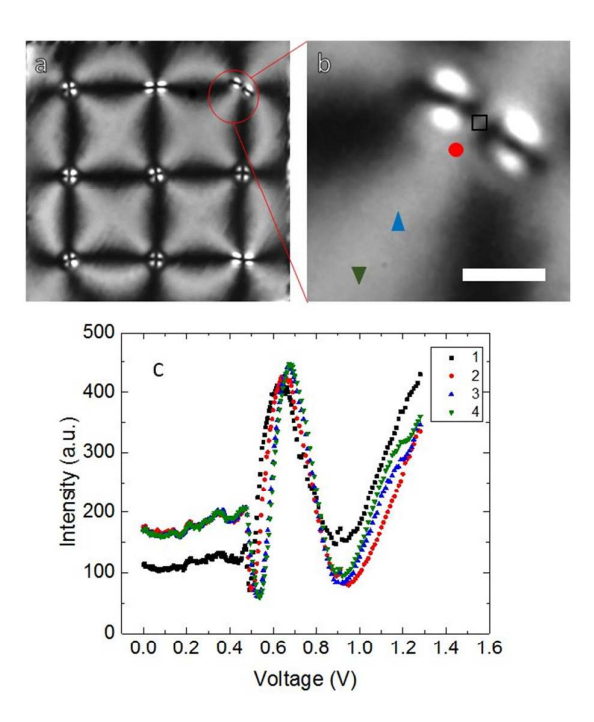


Fig. 10 Same as Fig. 9, except highlighting a *split* defect perpendicular to the midpoint between the two $m = +\frac{1}{2}$ daughter defects. Scale = 5 μ m.

applied voltage for the d = 7.5 μ m pattern. As the voltage is increased from zero, the dark ring (which corresponds to $\alpha=4\pi$) moves outward and a new dark ring corresponding to $\alpha=2\pi$ appears near the defect core. This behavior is

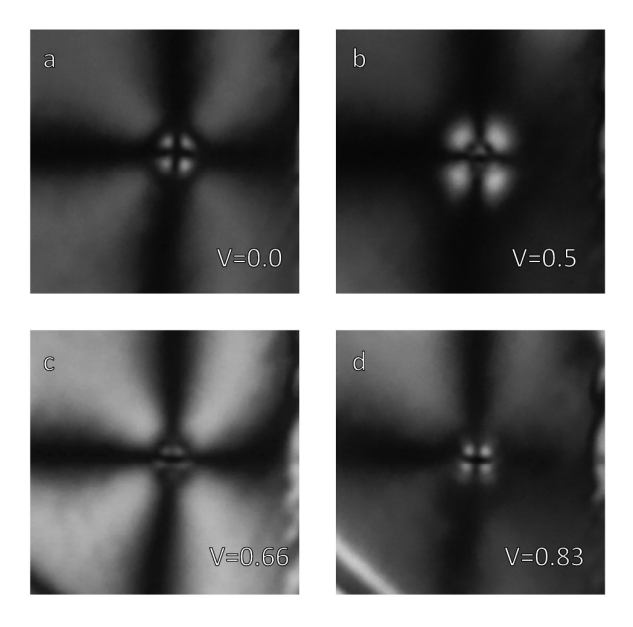


Fig. 11 A partially escaped m = -1 defect for the d = 7.5 μ m sample (same as Fig. 9) as a function of applied voltage. a) Dark ring corresponds to retardation α = 4π . As voltage increases, the director tends to orient more closely parallel to the z-axis in the defect core and the ring moves outward. A second ring corresponding to α = 2π begins to appear in (c) and is fully developed in (d).

indicative of a partially escaped director at V = 0.

We now focus on the middle defect along the top row of Fig. 9a, which has split into a pair of $m = -\frac{1}{2}$ defects. Here we do not see a dark ring surrounding the four spots. Instead there is a direct transition from each of the four bright spots to the less bright inter-defect region, without passing through a dark ring. This can be observed for split defects in all samples, and we will return to the issue of brightness level at the end of the Discussion section. Consider the bright spot in Fig. 3b (under the black open square marker); again, the integer defect has split into a pair of $m = +\frac{1}{2}$ defects. In Fig. 3c for corresponding voltage profile, one can see that there is an almost sharp Freedericksz threshold voltage. Freedericksz threshold is not possible in an escaped configuration, as an increasing applied voltage would result in a smoothly increasing torque on the director, which in turn would result in a smoothly varying intensity at that point in the sample. Figure 4 shows data for the same patterned square as in Fig. 3, but for a different defect, viz., at the center of the array. In this case the defect has not split into a pair of halfinteger defects, but rather possesses an escaped m = +1 core. The escape behavior is most readily seen in Fig. 4c, which shows a broad rounding of the intensity vs. voltage curve near the core region, which indicates a significant out-of-plane component of the director, even at V = 0. On the other hand, the much sharper Freedericksz transition of the bright spot in Fig. 3c demonstrates that this (i.e., the defect highlighted in Fig. 3a) is not an escaped region.

We then examined the d = 3.1 μ m sample as a function of temperature at V = 0. Images were recorded from room temperature at T = 23.9 °C through the nematic phase to

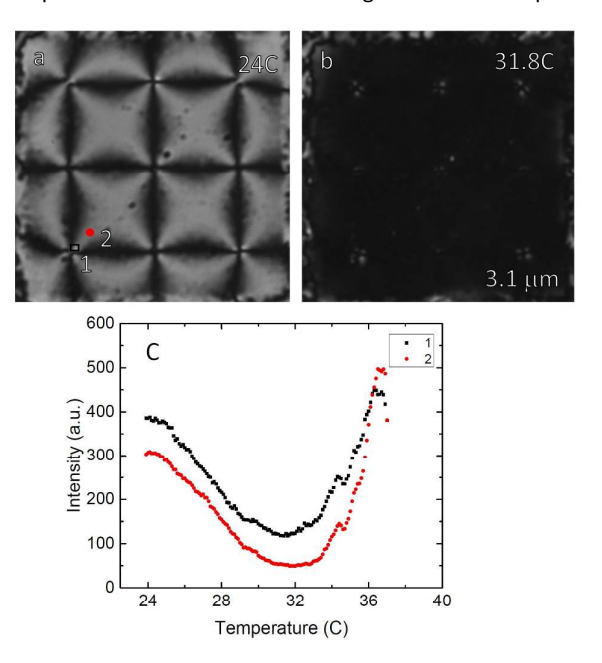


Fig. 12 Polarizing microscope images of $d=3.1~\mu m$ cell at T = 24 °C (a) and T = 31.8 °C (b). Figure (c) shows the intensity as a function of temperature at the two locations noted in (a).

isotropic phase transition at T_{NI} = 37.0°C every 0.1 °C as the

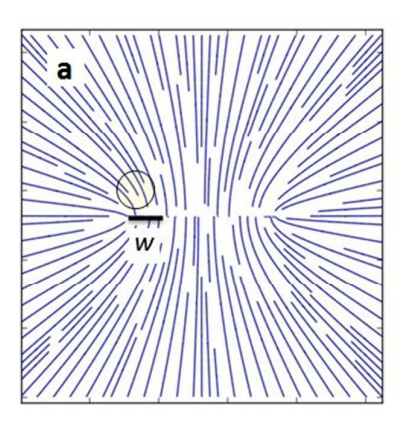
temperature was ramped at 0.5 °C min⁻¹. The images were analyzed at 131 different temperatures, two of which are shown in Fig. 12a and 12b. In Fig. 12a the inter-defect region has a total optical retardation $\alpha = 2\pi\Delta nd/\lambda = 7.6$ that renders strong intensity contrast, where the brightness $I \propto$ $(1-cos\alpha)sin^22\theta$ [18]. (For now, we also assume that θ (which is defined relative to the polarizer orientation) at a given position x,y is independent of height z in the cell.) As the temperature is increased, resulting in a decrease of the uniaxial nematic order parameter, both the diagonal interdefect region (position 2 in Fig. 12) and the spots (position 1) become dimmer. Nevertheless, the spots remain distinct and, in fact, tend to remain less dim than the inter-defect region. Eventually, at $T \sim 31.8^{\circ}$ C, where the nematic order parameter $S \sim 0.3$ [Ref. 19] and birefringence $\Delta n = 0.16$ [Ref. 19], the entire sample - except for the spots - becomes dark. [Here "dark" corresponds to the background intensity, as discussed above in conjunction with Fig. 3c.] This corresponds to a retardation $\alpha = 2\pi$. At still higher temperatures both the interdefect regions and the spots become brighter, but eventually the entire sample becomes dark at the isotropic transition temperature. We remark that the spot positions do become dark for an escaped integer defect. In fact, the spots actually translate radially, analogous to the voltage behavior in Fig. 11. This occurs because the temperature-dependent retardation depends on the in-plane component of the director, which is a function of the radial position relative to the defect center.

We note that only the master substrate is patterned, whereas the opposing substrate is planar degenerate, with a near-zero azimuthal anchoring strength — at least until a surface memory effect sets in²⁰. Split defects of the same sign, like charges, repel each other. Thus, we would expect the disclination line connecting the two surfaces to tilt away from each other²¹, as the half-integer defect cores at the slave surface are not pinned (as strongly) as compared to those at the master surface. With the assumption that there is no z component of the director for the split defects, and now relaxing our previous assumption that θ at a given position x,yis independent of z, we have mapped the planar director orientation θ as a function of z. The director \widehat{n} rotates strongly from the master to slave surface near the projection of the disclination line onto the xy-plane; see the circled areas in Figs. 13a and 13b, representing the director near a pair of split $m = +\frac{1}{2}$ defects in a plane at the patterned lower substrate (Fig. 13b) and at to the upper slave substrate (Fig. However, for a given position x,y far from the disclination line projection, the director \widehat{n} undergoes only negligible rotations $\delta\theta$ along the z-axis. Now, the linearly polarized light that enters the cell breaks into both ordinary and extraordinary components — the relative weights of the two components depend on the local director orientation and each polarization eigenvector rotates approximately with the director. But because the optical phase retardation corresponds to 2π at $T = 31.8^{\circ}$ C for the cell in Fig. 12, the light that exits the cell also is linearly polarized. Far from the projection into the xy-plane of the disclination line that connects the defect cores at the two substrates, there is very

little director rotation along the z-axis, and the crossed polarizer prevents the light from passing. But close to this disclination line the director undergoes a significant rotation $\delta\theta$ — see circled regions in Figs. 13a and 13b — permitting light to pass through the analyzer and resulting in the bright spots at a temperature when the rest of the cell is dark. We note that the projection into the xy-plane of the disclination line itself remains dark because the director reorients discontinuously by approximately 90° at the disclination line: The purely ordinary optical polarization that enters the cell abruptly shifts to purely extraordinary eigenmode, and thus does not pass through the analyzer.

Based on this behavior, we can determine the lateral separation w of a split defect at the top and bottom surfaces. Importantly, no potentially perturbing dye is needed here, as would be required for a confocal microscopy measurement. Let us focus first on point 2 (the red dot) in the inter-defect region at room temperature (when $\alpha \sim 7.6$) in Fig. 12a and the data in Fig. 12c. The intensity I due to retardation is $I = \frac{1}{2}I_0(1 - \cos\alpha)\sin^2 2\theta.$ The $sin^2 2\theta$ factor approximately equal to 1 at positions 1 and 2 in Fig. 12, where the director is $\theta \approx 45^\circ$ from the polarizer. We can fit the remaining cosine term, plus an offset, using the appropriate temperature dependence of Δn . From that fit, we determine a numerical value for I_0 . Now consider point 1 (the open square) that corresponds to the bright spot in Fig. 12 and the data in Fig. 12c at $T = 31.8^{\circ}$ C. Since the optical retardation at this temperature is 2π , the intensity would be zero if the director orientation θ were constant along the z-axis. But this is not necessarily the case — the director at position x,y rotates by an angle $\delta \theta$ from one substrate to the other if the defect cores are laterally displaced, much more so close to the defect; see Fig. 13. In light of Malus' law from which we deduce $I = I_0 sin^2 \delta\theta$, we measured I at its maximum in the bright spot, whence we obtain the director rotation $\delta\theta$ ~ 26° through the cell at the bright spot. From our director field mapping, this rotation $\delta \theta$ corresponds to a lower limit for lateral displacement $w = 1.2 \mu m$ for the disclination line separating the half-integer defect cores at the two substrates (Fig. 13). The reason for this being a lower limit for w is the intensity I vanishes at the disclination line, i.e., along the midline between the two bright spots, for the optical reasons described above, where $\delta\theta$ = $\pi/2$ along this line. Thus, the intensity of the bright spots actually is slightly less than that predicted by Malus' law, and our calculation for w represents a lower limit.

Finally, we remark that the intensity throughout each patterned region is determined by several factors: the optical retardation α and the azimuthal angle θ with respect to the polarizers, as well as any rotation $\delta\theta$ that exists between the two substrates in the region near a split defect. Consequences of this rotation were discussed above in detail. We have calculated a theoretical intensity map in the diffraction-free approximation as a function of α , θ , and $\delta\theta$. Over the parameter space of our experiment, i.e., for all values of α and θ and for relevant values of $\delta\theta$, our calculations show that the spots near the defect cores have an intensity close to or



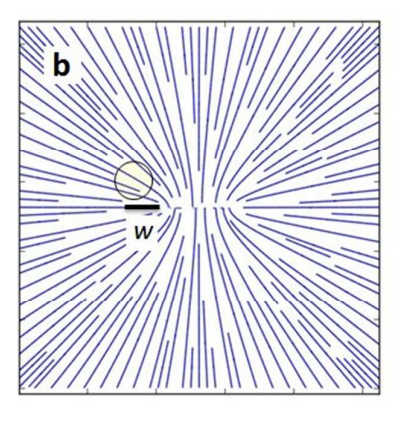


Fig. 13 Schematic representation of director profile associated with of a pair of $m=\pm 1$ defect lines at (a) the upper slave surface and (b) the bottom master surface. Circled region shows rotation $\delta\theta$ of the director from bottom to top surface. The dark line shows the projection of the disclination line (having length w) into the xy-plane.

greater than that in the inter-defect region. This is intuitively obvious for the case $\alpha=2\pi$ (Fig. 12b), but also holds true for all other values of $\alpha,\,\theta,$ and $\delta\theta$ probed in our experiments. As an aside, we point out that the spots often appear brighter to the eye than they actually are, as determined by quantitative analysis of the images. This is a perceptual illusion because the bright spots are surrounded closely on three or four sides by dark regions.

4 Conclusions

The results presented herein show evidence that defect decomposition is a preferred mechanism for defect energy relaxation in thinner nematic cells, whereas director escape (or partial escape) tends to be preferred in thicker cells. Additionally, we were able to measure the lateral displacement of the defect cores at the master and slave substrates that arises because of differences in anchoring at the two substrates. Although there are extant models that consider escape, defect decomposition, order reconstruction, and weakened nematic order (and ultimately melting) either

individually or as paired mechanisms, clearly there is a need for a more robust theory in three dimensions involving all of these mechanisms.

Acknowledgements

BSM was supported by the National Aeronautics and Space Administration under grant NNX17AC76G. CR was supported by the national Science Foundation's Condensed Matter Physics program under grant DMR1505389. SK acknowledges financial support from the Slovenian Research Agency, research core funding No. P1-0099.

20 N. Clark, *Phys. Rev. Lett.* 1985, **55**, 292
21 A. S. Backer, A. C. Callan-Jones, and R. A. Pelcovits, *Phys. Rev. E* 2008, **77**, 021701

Notes and references

- 1 W. H. Zurek, Nature 1985, 317, 505
- 2 M. Kleman and O.D. Lavrentovich, Soft Matter Physics, Springer-Verlag, New York 2003
- 3 P.J. Ackerman, Z. Qi, and I.I. Smalyukh, Phys. Rev. E 2012, 86, 021703 (2012)
- 4 Y.B. Guo, M. Jiang, C.H. Peng, K. Sun, O. Yaroshchuk, O. Lavrentovich, and Q.H. Wei, *Adv. Mater.* 2016, **28**, 2353
- 5 B.S. Murray, R.A. Pelcovits, and C. Rosenblatt, *Phys. Rev. E* 2014, **90**, 052501 (2014)
- S. Kralj, B.S. Murray, and C. Rosenblatt, *Phys. Rev. E* 2017, 95, 042702
- 7 R.J. Ondris-Crawford, G.P. Crawford, S. Zumer, and J.W. Doane, *Phys. Rev. Lett.* 1993, **70**, 194
- 8 P.E. Cladis, M. Kleman, J. Phys. France 1979, 40, 325
- 9 C. Chiccoli, I. Feruli, O.D. Lavrentovich, P. Pasini, S.V. Shiyanovskii, and C. Zannoni, *Phys. Rev. E* 2002, **66**, 030701
- 10 I.I. Smalyukh, R. Pratibha, N.V. Madhusudana, and O.D. Lavrentovich, *Eur. Phys. J. E* 2005, **16**, 179
- 11 I.F. Lyuksyutov, Sov. Phys. JETP 1979 48, 178-179 [Zh. Eksp. Teor. Fiz. 1978, 75, 358]
- 12 N. Schopohl and T.J. Sluckin, *Phys. Rev. Lett.* 1987, **59**, 2582-2584 (1987)
- 13 E. Pereira and F. Moraes, Liq. Cryst. 2011, 38, 295
- 14 S. Harkai, B.S. Murray, C. Rosenblatt, and S. Kralj (unpublished)
- 15 I.M. Syed, G. Carbone, C. Rosenblatt, and B. Wen, J. Appl. Phys. 2005, 98, 034303
- 16 J. Schindelin, I. Arganda-Carreras, E. Frise, et al, *Nature Methods 2012*, **9**, 676
- 17 B. Wen and C. Rosenblatt, J. Appl. Phys. 2001, 89, 4748-4751
- 18 B. Wen, M.P. Mahajan, and C. Rosenblatt, *Appl. Phys. Lett.* 2000, **76**, 1240
- 19 P.P. Karat and N.V. Madhusudana, *Mol. Cryst. Liq. Cryst.* 1976, 36, 51 (1976)